



# Aptasensing of beta-amyloid ( $A\beta_{(1-42)}$ ) by a 3D-printed platform integrated with leaf-shaped gold nanodendrites

Masoud Negahdary<sup>a,\*</sup>, William Barros Veloso<sup>a</sup>, Raphael Prata Bacil<sup>a</sup>, Rafael Martos Buoro<sup>b</sup>, Ivano Gebhardt Rolf Gutz<sup>a</sup>, Thiago Regis Longo Cesar Paixão<sup>a</sup>, Claudimir Lucio do Lago<sup>a</sup>, Solange Kazumi Sakata<sup>c</sup>, Gabriel Negrão Meloni<sup>a</sup>, Mesaque Carvalho França<sup>a</sup>, Thawan Gomes de Oliveira<sup>a</sup>, Wilson Akira Ameku<sup>a</sup>, Michelangelo Durazzo<sup>c</sup>, Lúcio Angnes<sup>a,\*</sup>

<sup>a</sup> Department of Fundamental Chemistry, Institute of Chemistry, University of São Paulo, Av. Prof. Lineu Prestes, 748, 05508-000 São Paulo, Brazil

<sup>b</sup> Institute of Chemistry of São Carlos, University of São Paulo, Av. Trabalhador São-Carlense, 400, 13556-590 São Carlos, Brazil

<sup>c</sup> Radiations Technology Center, Nuclear and Energy Research Institute (IPEN/CNEN - SP), São Paulo, SP, 05508-000, Brazil

## ARTICLE INFO

### Keywords:

Aptasensor  
Alzheimer's disease  
Beta-amyloid ( $A\beta_{(1-42)}$ )  
Bioelectrochemical assay  
3D-printed electrode  
Laser pyrolysis  
Leaf-shaped gold nanodendrites (LSG NDs)

## ABSTRACT

In this study, beta-amyloid ( $A\beta_{(1-42)}$ ), an essential biomarker for diagnosing Alzheimer's disease (AD), was detected via an electrochemical aptasensing platform. Here, an innovative signal transducer was developed using a CO<sub>2</sub> laser-ablated 3D-printed electrode modified with leaf-shaped gold nanodendrites (LSG NDs, mean diameter: ~ 92 nm), which could provide an efficient interface for immobilizing aptamer strands. The modified electrode with LSG NDs exhibited an enhancement in its electrochemically active surface area about 7 times, compared with the bare electrode. This modification showed that the size, morphology, and distributions of LSG NDs in amplifying electrochemical signals might effectively provide a highly sensitive infrastructure for analyte detection. The strands of a thiol-functionalized aptamer sequence interacted with the gold surface, which created an optimized biointerface to detect  $A\beta_{(1-42)}$  in a linear range from 0.1 pg mL<sup>-1</sup> to 10 ng mL<sup>-1</sup> (limit of detection (LOD): 84 fg mL<sup>-1</sup>, (S/N = 3)). The developed aptasensor confirmed satisfactory stability, desired reproducibility and regeneration, and minimal impact of interfering agents. In addition, the application of this aptasensor was monitored via an assay of spiked analyte concentrations in 20 samples, including cerebrospinal fluid (CSF) and human serum.

## 1. Introduction

Alzheimer's disease (AD) is the leading cause of dementia. There are no clear reasons for AD occurrence, but this disease has some critical risk factors such as age over 65 years, genetics (presence of the APOE-4 gene), patients with Down syndrome, some gene mutations, and family history [1,2]. The development of AD leads to the abnormal accumulation of  $A\beta$  peptides (mainly  $A\beta_{(1-40)}$  and  $A\beta_{(1-42)}$  subtypes) and tau proteins (phosphorylated and total types), causing the loss of normal neurons [3,4]. Plaques formed by these peptides and proteins disrupt normal neuron synapses due to the development of  $A\beta$  plaques outside the neurons or abnormal accumulation of tau protein inside the neurons [5]. Accessible levels of  $A\beta$  oligomers and tau proteins in cerebrospinal fluid (CSF) and blood are essential biomarkers for diagnosing and prognosis of AD [6,7]. In AD, biological changes in the brain, such as

developing  $A\beta$  oligomers, occur before reaching accumulated proteins or behavioral symptoms in patients. So, quantifying the level of AD biomarkers can be extremely effective in the early diagnosis and control of this disease, which is a promise for increasing the survival rate of patients [8,9]. Neuropathology examination of the brain is performed as the gold standard for AD diagnosis, which includes functional magnetic resonance imaging [10], positron emission tomography [11], computed tomography [12,13], and analysis of biofluids (CSF and blood content) [7]. Detecting biomarkers in biofluids provides rapid diagnosis, reduces costs, and can even be a quantitative, wide, and more practical diagnostic modality [14,15]. Compared to other diagnostic methods, electrochemical biosensors have some important advantages, including simple and low-cost design, portability, the possibility of miniaturization, and the feasibility of modifications in interface components [16–19]. Aptasensors provide the finest detections since they are

\* Corresponding authors.

E-mail addresses: [mnegahdary@iq.usp.br](mailto:mnegahdary@iq.usp.br) (M. Negahdary), [luangnes@iq.usp.br](mailto:luangnes@iq.usp.br) (L. Angnes).

<https://doi.org/10.1016/j.snb.2023.134130>

Received 26 March 2023; Received in revised form 4 June 2023; Accepted 9 June 2023

Available online 12 June 2023

0925-4005/© 2023 Elsevier B.V. All rights reserved.

equipped with unique aptamer sequences; this type of biorecognition element has several advantages, such as small size, high stability, and high affinity (electrostatic, van der Waals and hydrogen bonding) for capturing analytes [18,19]. So far, various electrochemical biosensors for A $\beta$  detection have been reported.

In a research, a biosensor was developed to detect several AD biomarkers, including Tau, ApoE4, A $\beta$ , and miRNA-101 [20]. A single-sided printed signal interface was utilized, while the working electrode area was made from a layer of Au. The surface of the working electrode was electrochemically modified with an array of gold nanodendrites. The electrodeposition conditions were optimized based on various potentials and deposition times, and  $-0.8$  V vs. Ag/AgCl for 800 s was selected as the optimum. The authors used only HAuCl<sub>4</sub>, which primarily can produce AuNPs, and to the best of our knowledge, producing other specific shapes and morphologies require some compatible additives such as biogenic amines [21–23], carbohydrates [24,25] or other biocompatible agents [16,18,26,27]. It is unfamiliar to produce gold nanodendrites just from a synthesis solution containing HAuCl<sub>4</sub>. In addition, the size and elemental analysis of the nanostructure were not reported. However, considering the present limitations for using antibodies [28,29], this biosensor showed good performance. In another research, a bare gold electrode was employed as the signal interface, and using thiol-functionalized aptamers an aptasensor was developed to detect ABO [30]. The electrochemical assays were performed using EIS, and the analytical results were satisfactory. Nevertheless, the application of other novel signal interfaces and advanced electrode surface modifiers, such as nanomaterial (s), is missing. In addition, the aptasensor assembly could be developed in more advanced platforms that authors have not followed; since several aptamer sequences were used, they could be employed in a sandwich-like platform or/and in the conjugated form with advanced materials such as nanomaterial (s). In a study, an APTS-Pt/Ti-glass substrate was employed as the signal transducer for biosensing A $\beta$ <sub>(1–42)</sub> [31]. The surface of this signal interface was modified with APTS and 1-ethyl-3-(3-dimethyl aminopropyl) carbodiimide hydrochloride (EDC) to be able to bound with amino-functionalized aptamer or antibody, and the authors claimed that the sensing performance is based on electrical capacitive coupling effect. While the authors obtained good results, this biosensor could be equipped with nanomaterial (s) and/or other assemblies such as multiplexed detection and sandwich-like platforms. In addition, the analytical performance could have been evaluated with common electrochemical techniques and in the same way for both conditions (immunosensor and aptasensor). In another research, a sandwich-like aptasensor equipped with molecular signal amplification and AgNPs was developed to detect ABO [32]. Here, a GE was employed as the signal interface and was treated with an aptamer sequence, and then various concentrations of analyte were added. Then, another aptamer sequence was added to the surface to establish the sandwich-like structure. Afterward, two hairpin DNA sequences capable of interacting with AgNPs were added to the surface, and electroanalytical assays were performed using linear sweep voltammetry. The authors reported good performance, but the surface of the used electrode could have been modified with advanced materials to deliver an enhanced electroactive surface area. In addition, other new signal transducers could be used. Electrochemical aptasensors have mostly been developed using commercially available glassy carbon, gold, and screen-printed electrodes [19,33,34]. The efficiency of these electrodes has been very satisfactory, and they are still widely used. However, one of the possibilities that can be employed to improve the diagnostic performance and reduce the design cost of aptasensors is using of three-dimensional (3D) electrodes, which is a scorching topic and may be used as an alternative over other electrodes in the design of electrochemical aptasensors [35–37]. These electrodes have important advantages that warrant their application. The most important advantages of these electrodes include low-cost design, improved electrochemical performance, and controllable modifications in the production materials [35,38,39]. One of the most important innovations in

electrochemical aptasensors is modifying the electrode surface with different nanomaterials. Recent research has shown that applying biocompatible nanomaterials based on gold and carbon has been widely considered [40–44]. The enhanced electroactive surface area of electrodes modified with nanomaterials is suitable for immobilizing the optimum volume of aptamer strands. Also, the extended surface allows a higher electron transfer rate and will provide amplified electrochemical signals.

In this research, we designed and produced a CO<sub>2</sub> laser-ablated 3D-printed platform electrode in which the electrode surface was modified with leaf-shaped gold nanodendrites (LSG NDs), creating a suitable option for interaction with the aptamer strands intended for A $\beta$ <sub>(1–42)</sub> detection. We demonstrate that this aptasensing platform is suitable for selective A $\beta$ <sub>(1–42)</sub> detection, paving the way for developing affordable AD diagnostic tools.

## 2. Materials and methods

All (bio) materials, reagents, and apparatus used are presented in the [Supplementary Materials](#).

### 2.1. Architecture and production of the 3D-printed electrode

The 3D-printed electrodes were fabricated as previously described elsewhere [45]. In brief, the electrodes comprised a conductive part, an electrode housing area, and an electrical contact ([Fig. S1a, b](#)). The conductive part was a cylindrical piece fabricated in a fused deposition modeling 3D printer using commercial conductive filaments of carbon black and polylactic acid (CB/PLA). The electrode housing was a non-conductive rectangular piece, printed in two halves and later glued together by masked stereolithography 3D printing. The main 3D printing parameters are presented in [Supplementary Materials](#).

### 2.2. Surface treatment of 3D-printed electrode by CO<sub>2</sub> laser-ablation

The process of CO<sub>2</sub> laser ablation has been confirmed to increase the electrical conductivity of 3D-printed electrodes by removing polymeric material from the electrode's surface [46,47]. Hence, a CO<sub>2</sub> laser (wavelength of 10.6  $\mu$ m) from a low-cost hobbyist laser engraver was used with power set to 1.6 Watts, laser scan rate of 20 mm s<sup>-1</sup>, and focal distance (distance between the laser emission and the substrate) of 7 mm. The total laser ablation time was 30 s

### 2.3. Preparation of A $\beta$ monomers (A $\beta$ Ms), A $\beta$ oligomers (A $\beta$ Os), and A $\beta$ fibrils (A $\beta$ Fs)

Different aggregation forms of A $\beta$  were prepared based on previous protocols with some modifications [48,49]. Briefly, 30  $\mu$ g lyophilized powder of A $\beta$ <sub>(1–42)</sub> was dissolved in 1 mL hexafluoroisopropanol (HFIP) and ultrasonicated for 15 min; then, the HFIP was evaporated using a flow of pure nitrogen, and the attained A $\beta$ Ms (30  $\mu$ g) was kept at  $-20$  °C before use. In order to prepare 30  $\mu$ g mL<sup>-1</sup> of A $\beta$ Os, the prepared A $\beta$ Ms (30  $\mu$ g) in the previous procedure were added to 1 mL of dimethylsulfoxide (DMSO). After 15 min ultrasonication, the achieved mixture was incubated in the refrigerator (4 °C) for 24 h. Finally, A $\beta$ Fs were prepared using a mixture of 30  $\mu$ g lyophilized powder of A $\beta$ <sub>(1–42)</sub> in 1 mL deionized (DI) water (Milli-Q Millipore 18.2 M $\Omega$  cm) and then incubated at 37 °C for seven days. Here, A $\beta$ Os (the most toxic form) were used as the analyte in all assays. Two nontoxic forms (A $\beta$ Ms and A $\beta$ Fs) were used for the selectivity assay.

### 2.4. Preparation of the aptasensing platform

After the 3D printed electrode was assembled and then ablated by the CO<sub>2</sub> laser, its surface was modified with a thin layer of LSG NDs via electrodeposition (Chronoamperometry, potential: 0 V and time: 300 s)

in the synthesis solution containing 20 mM HAuCl<sub>4</sub>, 0.5 M H<sub>2</sub>SO<sub>4</sub>, 75 mM spermine, and 75 mM histamine dissolved in water (Fig. S1c). Electrodes were then dried under a nitrogen flow and characterized electrochemically (using cyclic voltammetry (CV), electrochemical impedance spectroscopy (EIS), and differential pulse voltammetry (DPV) techniques). Then, the surface morphology and distribution of LSG NDs were characterized by field emission scanning electron microscopy (FESEM). Also, in another characterization, the chemical composition of the electrode surface was analyzed by an energy-dispersive X-ray spectrometer (EDS). A high-affinity [50] aptamer (24 mer oligonucleotide: 5'-GCCTGTGGTGTGGGGCGGGTGGC-3') was chosen as the biorecognition element for A $\beta$ Os (analyte) and received while 5' end was thiol-functionalized (Table S1). The aptamer concentration for immobilization on the surface of the electrode was calibrated to be 10  $\mu$ M. In order to activate the aptamer strands for immobilizing on the electrode surface, the thiol groups were cleaved via treatment with a dithiothreitol (DTT) mixture solution (500 mM DTT and 10 mM sodium acetate, pH 5.2) at room temperature for 20 min. Afterward, the mixture solution was washed thrice with ethyl acetate (300  $\mu$ L total) to eliminate excess DTT. 20  $\mu$ L of activated aptamer mixture solution was dropped on the electrode surface and kept at 4  $^{\circ}$ C for the desired time obtained through the open circuit potential (OCP) technique [16,18,21,51]; more information about aptamer characterization is presented in Supplementary Materials (section 8). In the next step, the electrode was treated with 20  $\mu$ L of 1 mM 6-mercapto-1-hexanol (MCH) and kept at room temperature for 30 min to block the nonspecific aptamer strands and improve the sensing performance by creating a self-assembled monolayer (via Au-S bond) of aptamer on the electrode surface. Then, various concentrations of A $\beta$ Os were added to the surface (electrode/LSG NDs/aptamer) and incubated at 37  $^{\circ}$ C for the desired time (the procedure and analysis details about the binding process between aptamer and analyte presented in Supplementary Materials).

All electrochemical measurements performed in a mixture of 0.5 M KCl and 0.5 mM ferro/ferricyanide (K<sub>4</sub>Fe(CN)<sub>6</sub>/K<sub>3</sub>Fe(CN)<sub>6</sub>) dissolved in 20 mM Tris(hydroxymethyl)aminomethane (Tris)-HCl pH 7.4 (calibrated with the aptasensor performance). An Ag/AgCl was employed as the reference electrode and a platinum wire was the counter electrode. All analytical measurements were performed using the DPV technique considering the following parameters:

Initial potential: 0 mV, end potential: 500 mV, step potential: 5 mV, modulation amplitude: 25 mV, modulation time: 0.05 s, interval time: 0.5 s, and scan rate: 10 mV s<sup>-1</sup>.

### 2.5. Evaluation of aptasensor performance

To evaluate the reproducibility, the aptasensor was reassembled six times, and for each time, a DPV was recorded. In order to repeat each cycle, biomolecules attached to the electrode surface were eliminated via 30 s washing with a piranha solution. The regeneration experiment was repeated six times, bounding the aptasensor with a concentration of analyte (0.05 ng mL<sup>-1</sup>), recording a DPV, and then cleaving the bound aptamer/analyte by inserting the aptasensor at a high temperature (95  $^{\circ}$ C) for 5 min and subsequently recording another DPV. The high temperature step was aimed to linearize the aptamer strands and release the analyte molecules from the aptasensing interface [52]. The stability performance was evaluated by providing the aptasensor interface bound with analyte (0.05 ng mL<sup>-1</sup>) and analyzing it for consecutive days. After recording each DPV, the aptasensor was refrigerated in 20 mM Tris-HCl (pH 7.4). In another experiment, the selectivity of the aptasensor was evaluated in the presence of several concentrations of analyte (A $\beta$ Os) and potential interfering agents (A $\beta$ M, A $\beta$ Fs, hemoglobin (Hb), and human serum albumin (HSA)) to find the possible interfering effect of them against the aptasensing performance. Finally, the performance of the aptasensor was evaluated by spiking various concentrations of A $\beta$ Os in artificial CSF (detail presented in Supplementary Materials) and human standard serum samples (50% diluted in phosphate-buffered

saline solution).

## 3. Results and discussion

### 3.1. Importance and principle of detection

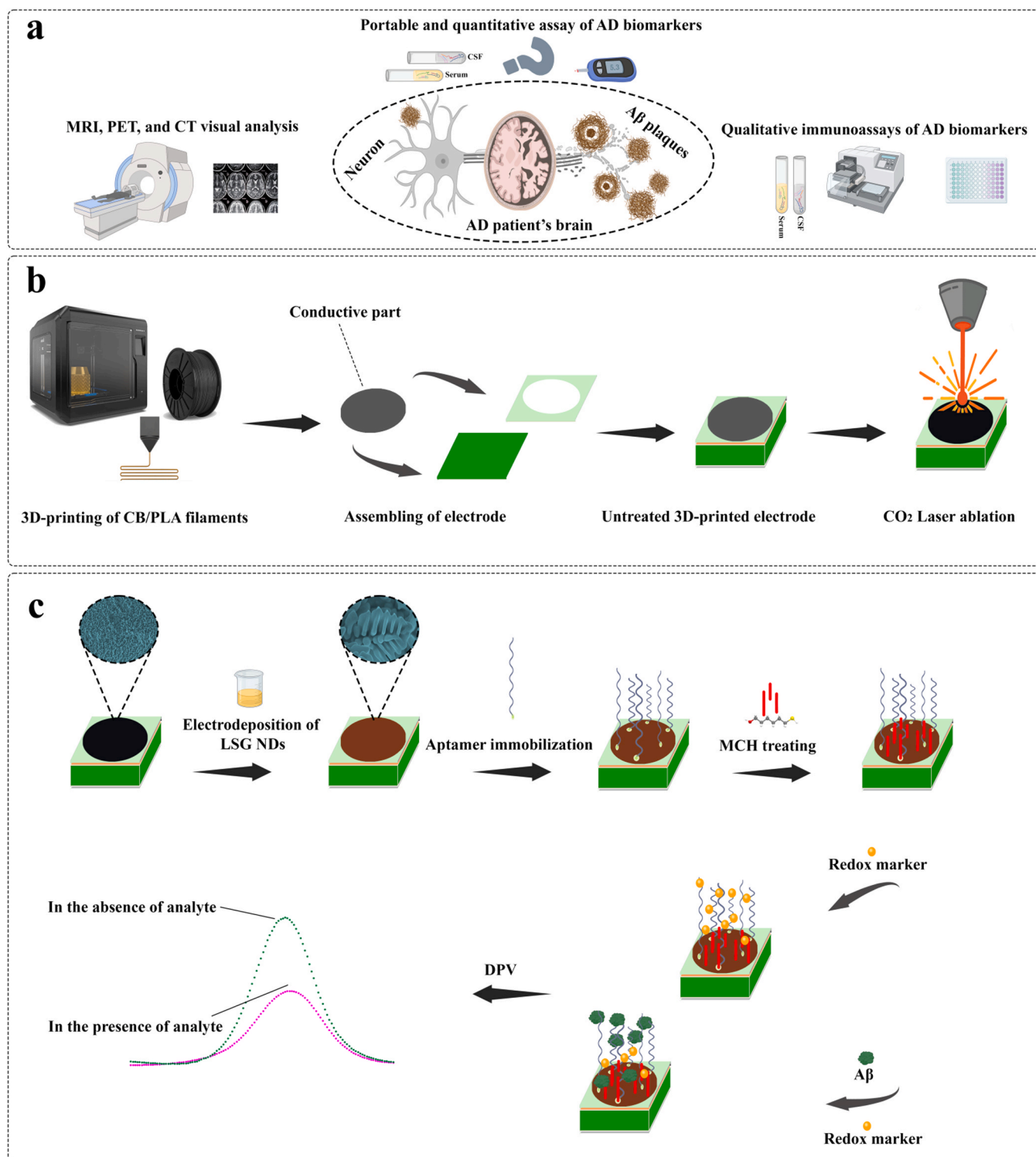
As shown in Fig. 1a, A $\beta$  plaques accumulate in the main structures of the brain, such as the hippocampus and cerebral cortex, in AD patients. There are three main paths for diagnosis. Referring patients to visual diagnosis based on tomography is one of the most common methods to show the extent of A $\beta$  accumulation. Unfortunately, this method is not effective in the early diagnosis of AD. The A $\beta$  level in CSF and serum is monitored mainly through immunoassay and other qualitative methods such as colorimetry. Due to the limitations of antibodies, non-portable equipment, and high-cost process, it is expected that aptasensors may become alternative products to early diagnosis of this disease (Fig. 1a).

Fig. 1b shows the design and production of the signal transducer, which started utilizing 3D printing of the CB/PLA filaments. The bare electrode preparation was then finalized by surface treatment with the CO<sub>2</sub> laser. In the next step, the primary surface modification of the electrode was performed by electrodeposition of LSG NDs, which led to a significant increase in the electrochemically active surface area (shown in the Supplementary Materials) and also provided a special surface for optimum immobilization of aptamer strands; the synthesized nanostructure greatly increased the diagnostic sensitivity (Fig. 1c). Next, the thiolated aptamer was immobilized on the surface through the bonding between thiol and gold. Then the aptamer immobilization process was conditioned by adding MCH. In this research, [Fe(CN)<sub>6</sub>]<sup>3-/4-</sup> was used as the redox marker. In the absence of the analyte, redox molecules had maximum access to the electrode surface, which led to higher DPV currents. In the presence of the analyte, due to the high affinity of the aptamer molecules against the analyte, the aptamer conformation was changed and trapped analyte molecules. Due to the large size of analyte molecules compared to redox molecules, the electrode surface's occupancy increased, hindering redox molecules' access to the electrode surface. In addition, the isoelectric pH of A $\beta$  was reportedly about 5.5 [53]. In analyte preparation solution pH (~ 7), A $\beta$  was negatively charged. Considering the net negative charge of the redox marker, an electrostatic repulsion was created on the electrode surface, which decreased the electron transfer rate. The steric and electrostatic repulsions had a linear relationship with analyte concentrations, which could provide a simple signal-off AD aptasensor.

### 3.2. Characterization of 3D-printed electrode modified by laser ablation and LSG NDs

#### 3.2.1. FESEM microscopy and EDS analysis

The surface morphology of the bare 3D-printed electrode was investigated by FESEM microscopy (Fig. 2a), and the micrograph of the surface confirmed a porous morphology with advantages such as improved reaction and material distribution that can interact with a higher rate of electrons leading to a significant increase in the charge transfer process compared to flat surface electrodes. Then, a thin layer of LSG NDs was electrodeposited on the electrode surface (Fig. 2b-f). The morphology of dendrites provided an enhanced and stable surface for immobilizing aptamer strands on the surface. Analysis of FESEM micrographs confirmed that the diameter of LSG NDs was between 63 and 137 nm with an average of 92 nm (Fig. S2 and Table S2); the average length of LSG NDs was about 570 nm. The applied potential (0 V) for electrodeposition was optimized to have the desired array of LSG NDs (Fig. 2g) [23,40,54]. The presence of biogenic amines (spermine and histamine), which are positively charged, acted as shape-directing agents and provided a homogeneous nanolayer of AuCl<sub>4</sub> ions via electrostatic interaction between the electrode surface and LSG NDs synthesis solution. In another analysis, the chemical composition of the modified surface with LSG NDs was evaluated by the EDS, and results



**Fig. 1.** Disruption in the functioning of neurons created by A $\beta$  plaques and possible diagnostic methods for AD (a); Design, production, assembly, and laser-ablation treatment for the 3D-printed electrode (b); and surface modification with LSG NDs and fabricating aptasensor platform (c).

confirmed a homogeneous gold distribution as the main (96.82%) element on the electrode surface (Fig. 2h, Fig. S3).

### 3.2.2. Electrochemical characterization of the electrode surface and preparation of aptasensing platform

The bare 3D-printed electrode and the modified electrode surface with LSG NDs were analyzed electrochemically via EIS, CV, and DPV. EIS spectra for the bare 3D-printed electrode were obtained in a range

from 100 kHz to 0.1 Hz and presented a first semi-circle in high frequencies that may be associated with the bulk resistance/ohmic drop (charge transfer resistance (RCT) = 1.74 k $\Omega$ ) (Fig. 3a and Fig. S4a). As the surface presented a high porosity (e.g., Fig. 2 c), the electrochemical probe infiltrates the pores, increasing the current obtained at the electrode surface and making ohmic drop the predominant phenomenon. While frequencies diminish, the increased time of the applied potential reduces the contribution of the pore-confined probe, and the interfacial

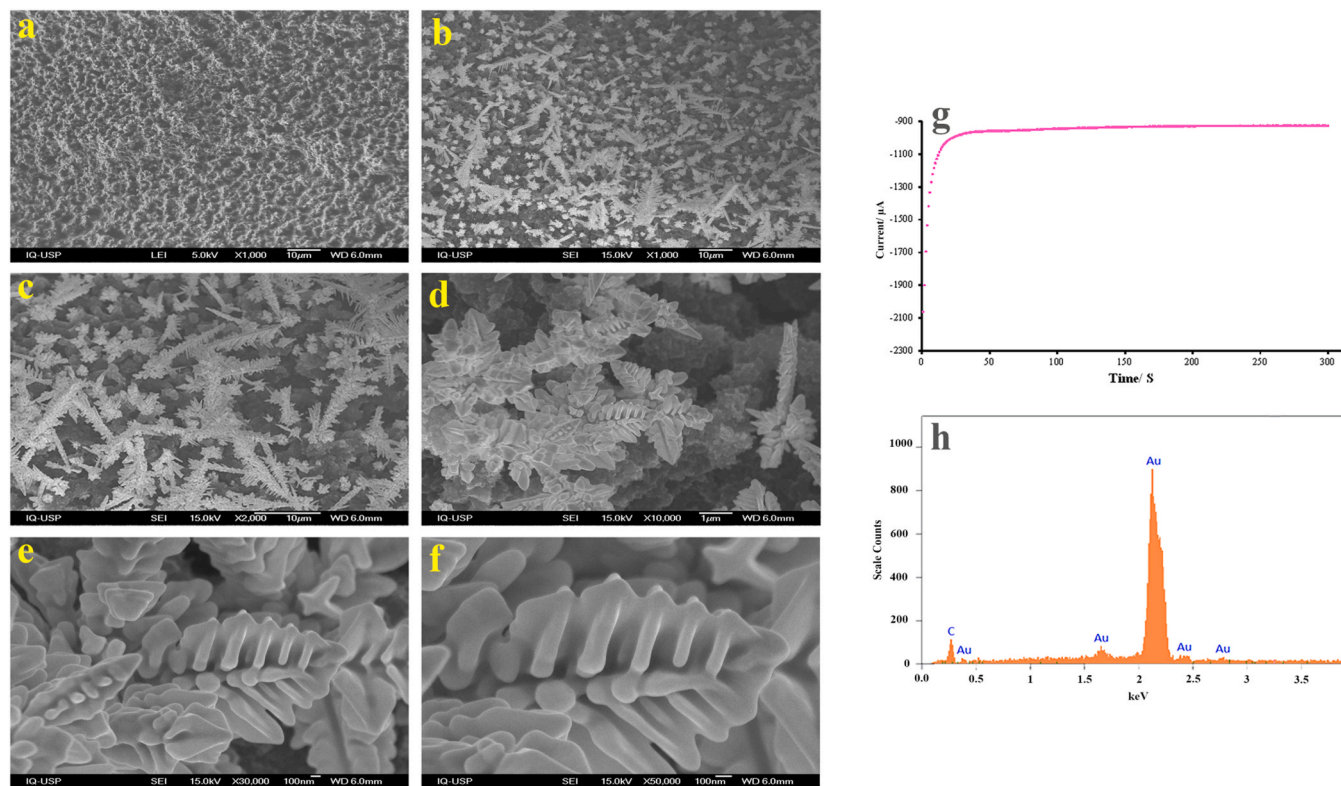


**Fig. 2.** Surface characterizations of the 3D-printed electrode: FESEM analysis of the bare electrode (a); FESEM analysis of the modified electrode with LSG NDs in different magnifications ( $\times 1000$  (b);  $\times 2000$  (c);  $\times 10000$  (d);  $\times 30000$  (e); and  $\times 50000$  (f); electrodeposition process of LSG NDs (g); and the EDS analysis of the modified electrode with LSG NDs (h).

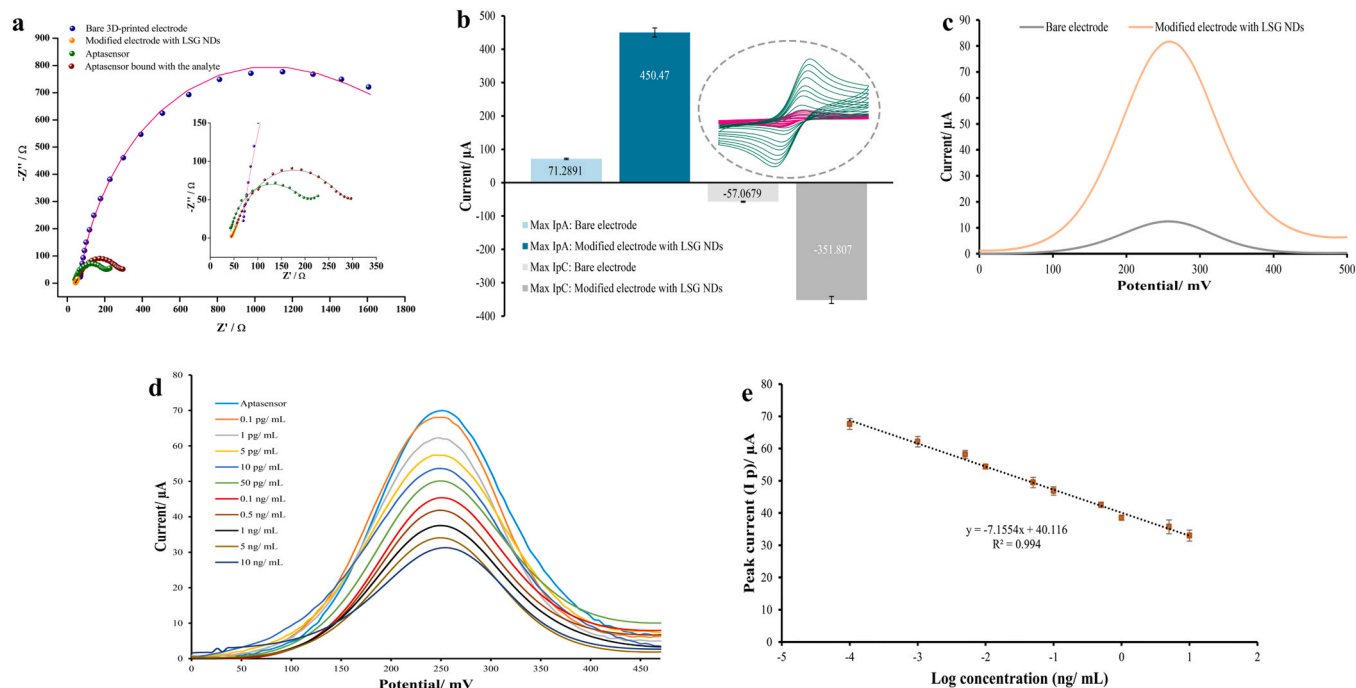


**Fig. 3.** Electrochemical characterization of the electrode surface: EIS analysis of the bare 3D-printed electrode, the modified electrode with LSG NDs, aptasensor, and aptasensor bound with the analyte (a); Ip anodic and Ip cathodic obtained from CV analysis related to the bare 3D-printed electrode and the modified electrode with LSG NDs (b); DPV analysis for bare 3D-printed electrode and the modified electrode with LSG NDs (c); DPVs related to the detection of various concentrations of A $\beta$ Os (d); and the calibration curve related to the logarithm of concentrations and DPVs peak currents (e); the error bars represent the SD of three repeated measurements (error bar: SD/ n = 3).

phenomena become predominant. This hypothesis is sustained as all spectra present a shift within the imaginary impedance ( $Z''$ -y axis), representing the transition from the predominance of bulk impedance to the interfacial impedance regardless of the electrode modification.

The EIS characterization for the modified electrode with LSG NDs was performed in a frequency range from 1 kHz to 1 Hz (Fig. 3a and Fig. S4b). The Randles circuit associated in series with the Warburg impedance ( $Z_w$ ) presented good fitting except for the modified electrode with LSG NDs in high decreased RCT (Table S3). However, this electrode presented a constant phase element in parallel with a resistor, associated with the RCT of the electrode, and a second constant phase element ( $CPE_2$ ) in substitution with the  $Z_w$  in the equivalent circuit (Fig. S5). The low phase angle of  $15^\circ$  supports the replacement of the  $Z_w$  in the equivalent circuit for the  $CPE_2$  observed in the Bode plot at low frequencies, which suggests a contribution from the electrode polarization in the total diffusional impedance. At the low-frequency range, diffusion is the predominant process contributing to the system's impedance, represented by the Warburg element.

In the constant phase element equation:

$$Z = \frac{1}{Y_0 j \omega^\alpha} \quad (1)$$

In which  $Y_0$  is associated with the capacitance,  $\alpha$  varies between 0 and 1, with 1 being a capacitor and 0 a resistor. When  $\alpha = 0.5$ , the CPE behaves as  $Z_w$  with a  $45^\circ$  phase angle observed at the Bode plot. In the capacitor,  $\alpha$  approaches 1 at low frequencies, representing the electrical charge of the double layer called equilibrium differential capacitance ( $C_{eq}$ ) [55]. The  $CPE_2$   $\alpha$  value of 0.619 suggests a predominant diffusional system but with a relevant contribution of the capacitance related to the surface electrical double layer due to the increased surface area of the modified electrode with LSG NDs.

For the aptasensor (electrode/LSG NDs/aptamer) and aptasensor bound with the analyte ( $0.05 \text{ ng mL}^{-1}$ ), the increase in the RCT is expected since these molecules hinder the charge transfer from the signal interface (discussed in Section 3.1 and shown in Fig. 3a and Fig. S4c, d). The found RCT for aptasensor and aptasensor bound with the analyte was  $0.156 \text{ k}\Omega$  and  $0.242 \text{ k}\Omega$ , respectively. All electrodes fit well to the proposed equivalent circuit with  $\chi^2$  between  $10^{-2}$  and  $10^{-3}$  (Fig. S5).

In another electrochemical characterization, the bare 3D-printed and the modified (with LSG NDs) electrodes were evaluated via CV analysis in scan rates ranging from 5 to  $300 \text{ mV s}^{-1}$ . The maximum anodic peak ( $I_p$ ) value for the bare 3D-printed electrode was  $\sim 71 \mu\text{A}$  (Fig. S6a). This value was found as  $\sim 450 \mu\text{A}$  for the modified electrode (Fig. S6b), confirming a significant enhancement in CV peak currents of the modified electrode with LSG NDs (Fig. 3b and Fig. S6d). In order to reach more features about the surface of both electrodes, electron transfer kinetic studies were performed (Supplementary Materials). Briefly, CVs of both electrodes confirmed quasi-reversible voltammograms. Through Randles-Sevcik equations, the real electroactive surface area ( $A$ ) was obtained for the bare 3D-printed electrode, about  $0.34 \text{ cm}^2$ , and this value for the modified electrode with LSG NDs was about  $2.38 \text{ cm}^2$ .  $\text{CO}_2$  laser treatment was performed on the bare electrode to remove unwanted insulating material, exposing electroactive carbon black sites and eventually providing a porous and compatible surface for modifying with LSG NDs, an optimum surface for immobilizing the biorecognition element. The charge transfer coefficient ( $\beta$ ) for both electrodes was 0.8 (Fig. S6d). In addition, the dimensionless function ( $\Psi$ ) was obtained as a function related to the difference of the peak potentials ( $\Delta E_p$ ) for each electrode separately, and also the  $\Psi$  reverse plot ( $\Psi \times \nu^{-1/2}$ ) was used to obtain the heterogeneous electron transfer constant ( $k^0$ ) (Table S4 and Fig. S6e). All other kinetics parameters are presented in the Supplementary Materials. The results confirmed that the surface modification with LSG NDs created a significant current increase (Fig. S7a, b and Table S5).

Fig. 3c shows DPVs for the bare 3D-printed and the modified (with LSG NDs) electrodes. Here,  $\Delta I$  ( $\Delta I = I_{\text{Modified electrode}} - I_{\text{Bare electrode}}$ ) was

$69.2 \mu\text{A}$  (the peak current gain ratio: 6.6) which shows the effectiveness of LSG NDs for improving the area and the conductivity of the electrode surface, rendering a robust signal amplification.

In an experiment, the OCP measurement was performed to determine the optimum time for immobilizing aptamer strands on the modified electrode surface with LSG NDs. The results showed enough time for the maximum aptamer immobilization processes was about 55 min (Fig. S8 and the procedure detail in Section 2.4). In addition, aptamer surface coverage ( $\Gamma$ ) was estimated to be  $7.046 \times 10^{12} \text{ molecules cm}^{-2}$  ( $11.7 \text{ pmol cm}^{-2}$ ) (detail presented in Supplementary Materials).

The optimum binding time was determined by evaluating the interaction between the aptasensor and  $0.05 \text{ ng mL}^{-1}$  of the analyte at  $37^\circ\text{C}$ , recording a DPV every 5 min till reaching the steady point of DPV peak currents. The corresponding time to the steady point was 20 min (Fig. S9 and the procedure detail in Section 2.4).

In addition, the binding affinity of aptamer for capturing the analyte molecules was estimated by determining the dissociation constant ( $K_D$ ), which was  $5.7 \pm 1.9 \text{ pM}$  (detail presented in Supplementary Materials; Fig. S10 and Table S6). The aptamer immobilized on the surface of the modified electrode with LSG NDs showed a very competitive affinity (considering the lower  $K_D$ ) against the analyte molecules compared to other research which they found  $K_D$  as  $111.64 \text{ pM}$  [56],  $3.4 \text{ nM}$  [57],  $20 \text{ nM}$  [58], and  $53.3 \text{ nM}$  [59].

### 3.3. Aptasensing of $A\beta$ Os

As shown in Fig. 3d, the aptasensor was evaluated at various concentrations of analyte and showed a linear decay of signal over a wide range from  $0.1 \text{ pg mL}^{-1}$  to  $10 \text{ ng mL}^{-1}$ . Hence, by enhancing analyte concentrations, the created steric and electrostatic repulsion on the electrode surface hindered the electron transfer of the redox marker at the interface. DPV peak current of the aptasensor (blank) was about  $70 \mu\text{A}$ . This value in the presence of the lowest and the highest evaluated concentrations of  $A\beta$ Os was  $67.6 \mu\text{A}$  and  $33 \mu\text{A}$ , respectively, which confirm a high conductive interface with enough enhanced electroactive surface area due to special morphology, size and distribution of LSG NDs on the surface. The calibration curve for the logarithmic presentation of concentrations and corresponding DPV peak currents is depicted in Fig. 3e. DPV peak current in the linear regression was  $(I_p)/\mu\text{A} = -7.16x \log C \text{ A}\beta\text{Os} + 40.1$ ,  $R^2 = 0.994$ . Here the limit of detection (LOD) ( $3\sigma/S$ ) and limit of quantification (LOQ;  $10\sigma/S$ ) were  $84 \text{ fg mL}^{-1}$  and  $136 \text{ fg mL}^{-1}$ , respectively, while  $\sigma$  was the standard deviations (SD) of blank signal in repeated assays, and  $S$  was as the slope of the linear equation ( $S/N = 3$ ).

In Table S7, all electrochemical aptasensors developed for detecting  $A\beta$  are inspected, and their main features are presented. However, compared to other research, the developed aptasensor in this research provided a wide detection range and a better or at least a competitive LOD due to the presence of a special assembly. The desired convergence was also found between the employed novel, simple, and optimal signal interface and the highly affinitive bioprobe against the analyte molecules.

### 3.4. Reproducibility, regeneration, and stability performance of aptasensor

To analyze the reproducibility, the developed aptasensor was rebuilt 6 times. A DPV was recorded each time, and the electrode was subsequently washed with the piranha solution for 30 s. The reproducibility evaluation showed a low relative standard deviation (RSD), about 1.3% (Fig. 4a and Fig. S11a).

In another experiment, a DPV was recorded for the aptasensor bound with  $0.05 \text{ ng mL}^{-1}$  of the analyte. Then the electrode was immersed in DI at a high temperature ( $95^\circ\text{C}$ ) for 5 min to change the conformation of aptamer strands and release the analyte molecules (debound status); a DPV was also recorded for debound status (Fig. S11b). This experiment

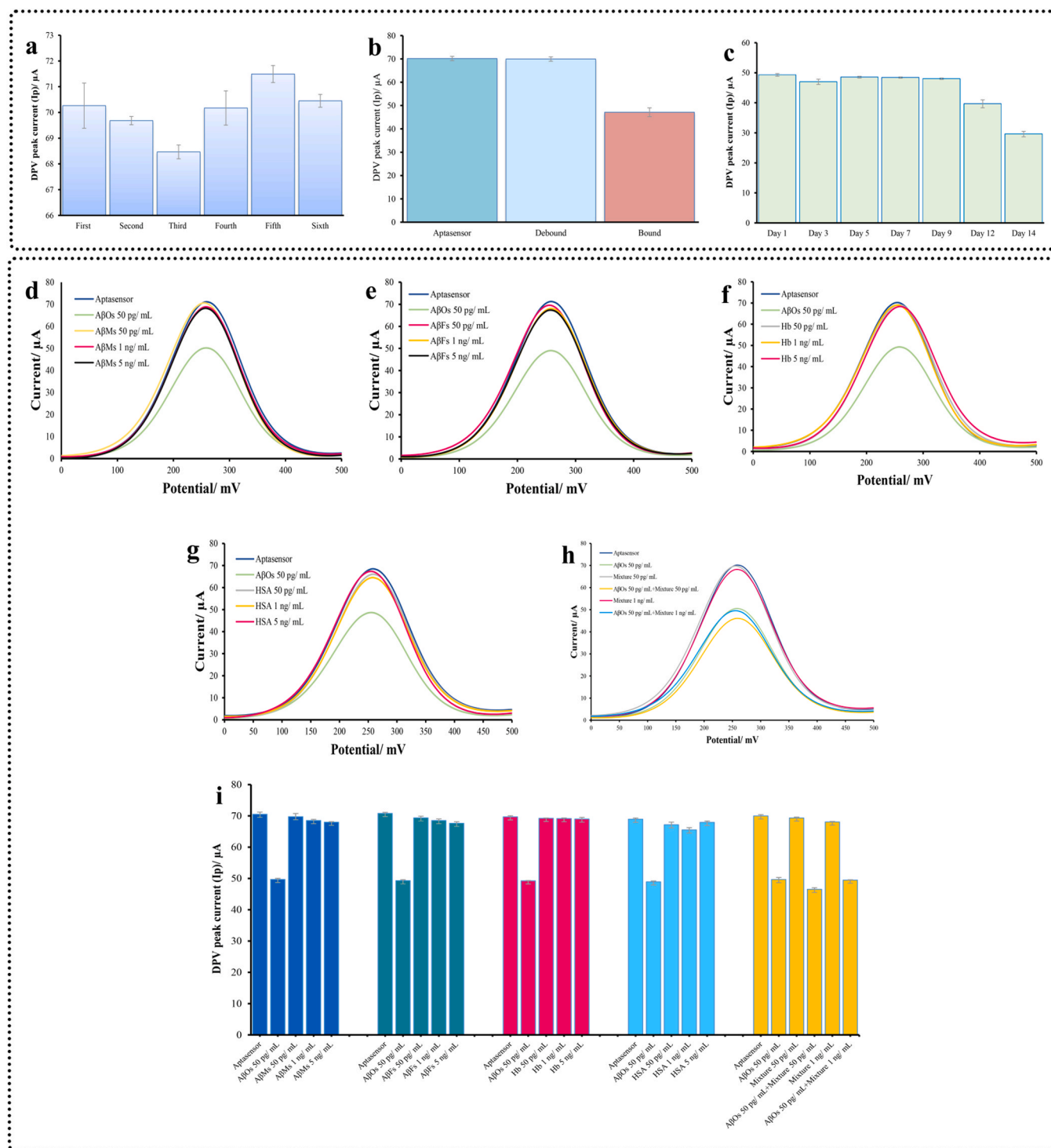


**Fig. 4.** Aptasensor performance for reproducibility (a); regeneration (b); stability (c); and the selectivity performance in the presence of A $\beta$ M $_1$  (d); A $\beta$ F $_1$  (e); Hb (f); HSA (g); and the mixture of interferences (h); the DPV peak currents of all groups (i); the error bars represent the standard deviations of three repeated measurements (error bar: SD/ n = 3).

was repeated 6 times, and the results confirmed a regenerative aptasensing platform (Fig. 4b), and the found RSD for bound and debound statuses were 3.9% and 1.3%, respectively).

The stability performance was evaluated for the aptasensor bounded with  $0.05 \text{ ng mL}^{-1}$  of the analyte, recording DPVs for consecutive days. The stability was confirmed for 9 days with an RSD of about 1.6% (Fig. 4c) and Fig. S11c). However, the  $\Delta I$  ( $\Delta I = I_{\text{First day}} - I_{\text{Day 12 or Day 14}}$ ) for day 12 and day 14 was 9.62 (19.52% loss of initial performance) and

19.78 (40.1% loss of initial performance), respectively.

### 3.5. Selectivity performance of aptasensor

The selectivity performance of the aptasensor was evaluated in the presence of several interferences (A $\beta$ M $_1$ , A $\beta$ F $_1$ , Hb, and HSA). Here, the analyte concentration was  $50 \text{ pg mL}^{-1}$ , while the concentrations of interfering species were  $50 \text{ pg mL}^{-1}$ ,  $1 \text{ ng mL}^{-1}$ , and  $5 \text{ ng mL}^{-1}$ . In

another condition, the mixture of interfering species and mixtures containing the interfering species + the analyte was analyzed (Fig. 4d-h). In this experiment,  $\Delta I$  ( $\Delta I = I_{\text{Aptasensor}} - I_{\text{interferences or analyte}}$ ) was used to present the differences between DPV peak currents. The  $\Delta I$  for A $\beta$ Os, A $\beta$ M, A $\beta$ F, Hb, HSA, the mixture of interferences, and the mixture of interferences/analyte were 20.7, 1.78, 2.29, 0.57, 2.07, 0.64, and 23.46  $\mu$ A respectively (Fig. 4i). The results confirmed that these agents, even in high concentrations, did not significantly affect the performance of this highly selective aptasensor.

### 3.6. Application of aptasensor

The accuracy of the developed aptasensor was evaluated via spiked concentrations of A $\beta$ Os in 10 CSF and 10 serum samples (Table 1). The recovery values for spiked concentrations in CSF samples were found between 96.3% and 110% (RSD: 4.3). Results for serum samples were found between 95.8% and 110.4% (RSD: 4.1). Both mediums confirmed the desired diagnostic performance, thus suggesting this aptasensing platform for assay of clinical samples.

## 4. Conclusion

Due to the recent advances in medicine and the significant enhancement in access to amenities, the lifespan has increased. However, an important disease that generally appears in the elderly is AD, which causes high treatment costs and challenges for patients and society. In summary, in this research, a new aptasensor has been designed to diagnose AD, which has important features and advantages that were not achieved in previous research: One: A special signal interface was developed using CO<sub>2</sub> laser-ablation 3D-printing technology which operated as the working electrode. This type of innovative signal transducer can be considered as an alternative for present commercial electrodes; two: modification of the electrode surface with LSG NDs established a large electroactive surface area for interaction with aptamer and redox marker molecules, which compared to the bare electrode, the electrochemical signals were greatly amplified; three: The optimum interactions recognized in aptasensor components such as the signal transducer, LSG NDs, and aptamer strands could provide a wide linear detection range, a low LOD, good selectivity, and high repeatability. Due to the high cost of commercial electrodes and the need for access to major changes and modifications in the production material, designing cheap and more optimal interfaces seems logical. The superior efficiency and simplicity in designing the developed aptasensor in this research is a valuable step to reaching early diagnostic platforms for AD.

### CRedit authorship contribution statement

**Masoud Negahdary:** conceptualization, main aptasensor experiments, original Draft, review and editing. **William Barros Veloso:** producing electrodes, writing some methods. **Raphael Prata Bacil:** analyzing some data, writing some parts. **Rafael Martos Buoro:** analyzing some data, writing some parts. **Ivano Gebhardt Rolf Gutz:** analyzing some data, review and editing. **Thiago Regis Longo Cesar Paixão:** supporting in electrode design and production, review and editing. **Claudimir Lucio do Lago:** supporting some steps in CSF preparation. **Solange Kazumi Sakata:** supporting EDS analyze. **Gabriel Negrão Meloni:** supporting in electrode design and production, review and editing. **Mesaque Carvalho França:** supporting in drawing some graphs. **Thawan Gomes de Oliveira:** analyzing some data. **Wilson Akira Ameku:** connection between groups, supporting in initial electrode tests. **Michelangelo Durazzo:** supporting EDS analyze. **Lúcio Angnes:** Funding acquisition, Resources, Supervision, review and editing.

**Table 1**

Evaluation the application of aptasensor in detecting various spiked concentrations of analyte in CSF and serum samples (n = 3).

Sample No.	Added A $\beta$ Os (pg mL <sup>-1</sup> )	Detected A $\beta$ Os (pg mL <sup>-1</sup> )	Recovery (%)
CSF 1	0.1	0.11 ± 0.04	110
CSF 2	1	1.06 ± 0.31	106
CSF 3	5	4.83 ± 0.22	96.6
CSF 4	10	9.63 ± 1.29	96.3
CSF 5	50	52.75 ± 2.47	105.5
CSF 6	100	97.38 ± 5.12	97.38
CSF 7	500	509.7 ± 8.02	101.94
CSF 8	1000	978.39 ± 13.77	97.83
CSF 9	5000	5074 ± 11.32	101.48
CSF 10	10000	1036 ± 44.98	103.6
Serum 1	0.1	0.103 ± 0.07	103
Serum 2	1	1.08 ± 0.09	108
Serum 3	5	5.31 ± 0.87	106.2
Serum 4	10	9.75 ± 2.31	97.5
Serum 5	50	47.90 ± 4.56	95.8
Serum 6	100	105.6 ± 6.18	105.6
Serum 7	500	502.6 ± 12.06	100.52
Serum 8	1000	1022 ± 8.54	102.2
Serum 9	5000	5195 ± 35.88	103.9
Serum 10	10000	1104 ± 76.32	110.4

### Declaration of Competing Interest

The authors declare that they have no known competing financial interests or personal relationships that could have appeared to influence the work reported in this paper.

### Data availability

Data will be made available on request.

### Acknowledgments

The authors would like to thank the Sao Paulo Research Foundation-FAPESP (projects 2019/27021–4, 2018/08782–1, 2017/13137–5, and 2014/50867–3) and the National Council for Research-CNPq (processes 311847–2018-8, 302839/2020–8, and 465389/2014–7). This study was financed in part by the Coordenação de Aperfeiçoamento de Pessoal de Nível Superior - Brasil (CAPES) - Finance Code 001. The authors are also appreciative to Central Analítica (IQ-USP), and Laboratório de Microscopia e Microanálise do Centro de Ciência e Tecnologia de Materiais do IPEN/CNEN-SP for material characterization facilities.

### Appendix A. Supporting information

Supplementary data associated with this article can be found in the online version at doi:10.1016/j.snb.2023.134130.

### References

- [1] J. Fortea, S.H. Zaman, S. Hartley, M.S. Rafii, E. Head, M. Carmona-Iragui, Alzheimer's disease associated with down syndrome: a genetic form of dementia, *Lancet Neurol.* 20 (2021) 930–942.
- [2] A.T. Mohammadi, M. Bahaeddini, N. Dehghani, N. Dehghani, S.G. Shafagh, R. Qahremani, et al., Alzheimer's disease: for Researchers, Springer, 2022.
- [3] S. Palmqvist, P. Tideman, N. Cullen, H. Zetterberg, K. Blennow, J.L. Dage, et al., Prediction of future Alzheimer's disease dementia using plasma phospho-tau combined with other accessible measures, *Nat. Med.* 27 (2021) 1034–1042.
- [4] H. Hampel, J. Hardy, K. Blennow, C. Chen, G. Perry, S.H. Kim, et al., The amyloid- $\beta$  pathway in Alzheimer's disease, *Mol. Psychiatry* 26 (2021) 5481–5503.
- [5] M.A. Busche, B.T. Hyman, Synergy between amyloid- $\beta$  and tau in Alzheimer's disease, *Nat. Neurosci.* 23 (2020) 1183–1193.
- [6] S. Hu, C. Yang, H. Luo, Current trends in blood biomarker detection and imaging for Alzheimer's disease, *Biosens. Bioelectron.* (2022), 114278.
- [7] C.E. Teunissen, I.M. Verberk, E.H. Thijssen, L. Vermunt, O. Hansson, H. Zetterberg, et al., Blood-based biomarkers for Alzheimer's disease: towards clinical implementation, *Lancet Neurol.* 21 (2022) 66–77.
- [8] P.M. Rossini, R. Di Iorio, F. Vecchio, M. Anfossi, C. Babiloni, M. Bozzali, et al., Early diagnosis of Alzheimer's disease: the role of biomarkers including advanced

- EEG signal analysis. report from the IFCN-sponsored panel of experts, Clin. Neurophysiol. 131 (2020) 1287–1310.
- [9] A. Porsteinsson, R. Isaacson, S. Knox, M. Sabbagh, I. Rubino, Diagnosis of early Alzheimer's disease: clinical practice in 2021, J. Prev. Alzheimer's Dis. 8 (2021) 371–386.
- [10] Y. Wu, X. Wu, L. Gao, Y. Yan, Z. Geng, S. Zhou, et al., Abnormal functional connectivity of thalamic subdivisions in Alzheimer's disease: a functional magnetic resonance imaging study, Neuroscience 496 (2022) 73–82.
- [11] C. Strikwerda-Brown, D.A. Hobbs, J. Gonneaud, F. St-Onge, A.P. Binette, H. Ozlen, et al., Association of elevated amyloid and tau positron emission tomography signal with near-term development of Alzheimer disease symptoms in older adults without cognitive impairment, JAMA Neurol. 79 (2022) 975–985.
- [12] P. Scheltens, Imaging in Alzheimer's disease, Dialogues in clinical neuroscience, (2022).
- [13] A. Cistaro, N. Quartuccio, L. Cassalia, D. Vai, U.P. Guerra, C. Atzori, et al., Brain 18F-Florbetapir PET/CT Findings in an Early-onset Alzheimer Disease Patient Carrying Presenilin-1 G378E Mutation, Alzheimer Dis. Assoc. Disord. 36 (2022) 347–349.
- [14] H. Hampel, K. Broich, Y. Hoessler, J. Pantel, Biological markers for early detection and pharmacological treatment of Alzheimer's disease, Dialog.- Clin. Neurosci. 11 (2009) 141–157.
- [15] J. Thériault, E.R. Zimmer, A.L. Benedet, T.A. Pascoal, S. Gauthier, P. Rosa-Neto, Staging of Alzheimer's disease: past, present, and future perspectives, Trends Mol. Med. 28 (2022) 726–741.
- [16] M. Negahdary, H. Heli, An electrochemical peptide-based biosensor for the Alzheimer biomarker amyloid- $\beta$ (1–42) using a microporous gold nanostructure, Microchim. Acta 186 (2019) 766.
- [17] J. Zamanian, Z. Khoshbin, K. Abnous, S.M. Taghdisi, H. Hosseinzadeh, N. M. Danesh, Current progress in aptamer-based sensing tools for ultra-low level monitoring of Alzheimer's disease biomarkers, Biosens. Bioelectron. 197 (2022), 113789.
- [18] M. Negahdary, H. Heli, An ultrasensitive electrochemical aptasensor for early diagnosis of Alzheimer's disease, using a fern leaves-like gold nanostructure, Talanta 198 (2019) 510–517.
- [19] M. Negahdary, L. Angnes, Electrochemical aptamer-based nanobiosensors for diagnosing Alzheimer's disease: a review, Biomat. Adv. 135 (2022), 112689.
- [20] Y. Song, T. Xu, Q. Zhu, X. Zhang, Integrated individually electrochemical array for simultaneously detecting multiple Alzheimer's biomarkers, Biosens. Bioelectron. 162 (2020), 112253.
- [21] M. Negahdary, M. Behjati-Ardakani, N. Sattarahmady, H. Yadegari, H. Heli, Electrochemical aptasensing of human cardiac troponin I based on an array of gold nanodumbbells-Applied to early detection of myocardial infarction, Sens. Actuators B: Chem. 252 (2017) 62–71.
- [22] M. Negahdary, L. Angnes, An aptasensing platform for detection of heat shock protein 70 kDa (HSP70) using a modified gold electrode with lady fern-like gold (LFG) nanostructure, Talanta 246 (2022), 123511.
- [23] M. Negahdary, M.H. Hirata, S.K. Sakata, R.M. Ciconelli, G.M. Bastos, J.B. Borges, et al., Sandwich-like electrochemical aptasensing of heat shock protein 70 kDa (HSP70): application in diagnosis/prognosis of coronavirus disease 2019 (COVID-19), Anal. Chim. Acta 1242 (2023), 340716.
- [24] R. Dehdari Vais, H. Heli, N. Sattarahmady, Label-free electrochemical DNA biosensing of MR TV 29 18s ribosomal RNA gene of Trichomonas vaginalis by signalization of non-spherical gold nanoparticles, Mater. Today Commun. 34 (2023), 105123.
- [25] R.D. Vais, N. Sattarahmady, H. Heli, Green electrodeposition of gold nanostructures by diverse size, shape, and electrochemical activity, Gold. Bull. 49 (2016) 95–102.
- [26] M. Negahdary, H. Heli, An electrochemical troponin I peptisensor using a triangular icicle-like gold nanostructure, Biochem. Eng. J. 151 (2019), 107326.
- [27] M. Negahdary, M. Behjati-Ardakani, H. Heli, An electrochemical troponin T aptasensor based on the use of a macroporous gold nanostructure, Microchim. Acta 186 (2019) 377.
- [28] S. Arshavsky-Graham, K. Urmann, R. Salama, N. Massad-Ivanir, J.-G. Walter, T. Scheper, et al., Aptamers vs. antibodies as capture probes in optical porous silicon biosensors, Analyst 145 (2020) 4991–5003.
- [29] H. Yoo, H. Jo, S.S. Oh, Detection and beyond: challenges and advances in aptamer-based biosensors, Mater. Adv. 1 (2020) 2663–2687.
- [30] Y. Zhang, G. Figueroa-Miranda, Z. Lyu, C. Zafiu, D. Willbold, A. Offenhäuser, et al., Monitoring amyloid- $\beta$  proteins aggregation based on label-free aptasensor, Sens. Actuators B Chem. 288 (2019) 535–542.
- [31] P.K. Sharma, E.-S. Kim, S. Mishra, E. Ganbold, R.-S. Seong, Y.M. Kim, et al., Ultrasensitive probeless capacitive biosensor for amyloid beta (A $\beta$ 1–42) detection in human plasma using interdigitated electrodes, Biosens. Bioelectron. 212 (2022), 114365.
- [32] X. Liao, K. Ge, Z. Cai, S. Qiu, S. Wu, Q. Li, et al., Hybridization chain reaction triggered poly adenine to absorb silver nanoparticles for label-free electrochemical detection of Alzheimer's disease biomarkers amyloid  $\beta$ -peptide oligomers, Anal. Chim. Acta 1192 (2022), 339391.
- [33] P. Lakhera, V. Chaudhary, A. Jha, R. Singh, P. Kush, P. Kumar, Recent developments and fabrication of the different electrochemical biosensors based on modified screen printed and glassy carbon electrodes for the early diagnosis of diverse breast cancer biomarkers, Mater. Today Chem. 26 (2022), 101129.
- [34] C. Erkmen, G.A. Tig, G. Marrazza, B. Uslu, Design strategies, current applications and future perspective of aptasensors for neurological disease biomarkers, TrAC Trends Anal. Chem. (2022), 116675.
- [35] M.A. Ali, C. Hu, E.A. Yttri, R. Panat, Recent advances in 3D printing of biomedical sensing devices, Adv. Funct. Mater. 32 (2022), 2107671.
- [36] D.P. Rocha, V.N. Ataíde, A. de Siervo, J.M. Gonçalves, R.A.A. Muñoz, T.R.L. C. Paixão, et al., Reagentless and sub-minute laser-scribing treatment to produce enhanced disposable electrochemical sensors via additive manufacture, Chem. Eng. J. 425 (2021), 130594.
- [37] M. Abdelkader, M. Elmanzalawy, R. Pauliukaite, 3-D electrodes for electrochemical sensors: review in different approaches, IEEE Sens. J. 22 (2022) 23620–23632.
- [38] Y. Jiang, M.N. Islam, R. He, X. Huang, P.F. Cao, R.C. Advincula, et al., Recent advances in 3D printed sensors: materials, design, and manufacturing, Adv. Mater. Technol. (2022), 2200492.
- [39] S. Shakibania, M. Khakbiz, C.K. Bektas, L. Ghazanfari, M.T. Banizi, K.-B. Lee, A review of 3D printing technology for rapid medical diagnostic tools, Mol. Syst. Des. Eng. 7 (2022) 315–324.
- [40] M. Negahdary, Electrochemical aptasensors based on the gold nanostructures, Talanta 216 (2020), 120999.
- [41] H. Ji, X. Kang, X. Yang, H. Chen, T. Mao, Y. He, et al., Functionalized graphene-based electrochemical array sensors for the identification of distinct conformational states of Amyloid Beta in Alzheimer's disease, Biosens. Bioelectron. 222 (2023), 114927.
- [42] J. Yi, Y. Xianyu, Gold nanomaterials-implemented wearable sensors for healthcare applications, Adv. Funct. Mater. 32 (2022), 2113012.
- [43] M. Bilal, M. Barani, F. Sabir, A. Rahdar, G.Z. Kyzas, Nanomaterials for the treatment and diagnosis of Alzheimer's disease: an overview, NanoImpact 20 (2020), 100251.
- [44] L. Li, R. He, H. Yan, Z. Leng, S. Zhu, Z. Gu, Nanotechnology for the diagnosis and treatment of Alzheimer's disease: a bibliometric analysis, Nano Today 47 (2022), 101654.
- [45] W.B. Veloso, T.R.L.C. Paixão, G.N. Meloni, 3D printed electrodes design and voltametric response, Electrochim. Acta (2023), 142166.
- [46] D.P. Rocha, V.N. Ataíde, A. de Siervo, J.M. Gonçalves, R.A. Muñoz, T.R. Paixão, et al., Reagentless and sub-minute laser-scribing treatment to produce enhanced disposable electrochemical sensors via additive manufacture, Chem. Eng. J. 425 (2021), 130594.
- [47] X. Han, Y. Zhang, J. Tian, T. Wu, Z. Li, F. Xing, et al., Polymer-based microfluidic devices: a comprehensive review on preparation and applications, Polym. Eng. Sci. 62 (2022) 3–24.
- [48] P. Wang, P.-P. Guan, X. Yu, L.-C. Zhang, Y.-N. Su, Z.-Y. Wang, Prostaglandin I<sub>2</sub> attenuates prostaglandin E<sub>2</sub>-stimulated expression of interferon  $\gamma$  in a  $\beta$ -amyloid protein-and NF- $\kappa$ B-dependent mechanism, Sci. Rep. 6 (2016) 1–16.
- [49] P. Wang, X. Yu, P.-P. Guan, J.-W. Guo, Y. Wang, Y. Zhang, et al., Magnesium ion influx reduces neuroinflammation in A $\beta$  precursor protein/Presenilin 1 transgenic mice by suppressing the expression of interleukin-1 $\beta$ , Cell. Mol. Immunol. 14 (2017) 451–464.
- [50] K. Tsukakoshi, K. Abe, K. Sode, K. Ikebukuro, Selection of DNA aptamers that recognize  $\alpha$ -synuclein oligomers using a competitive screening method, Anal. Chem. 84 (2012) 5542–5547.
- [51] R. Nazari-Vanani, N. Sattarahmady, H. Yadegari, M. Khatami, H. Heli, Electrochemical biosensing of 16s rRNA gene sequence of Enterococcus faecalis, Biosens. Bioelectron. 142 (2019), 111541.
- [52] T.A. Tockary, W. Foo, A. Dirisala, Q. Chen, S. Uchida, S. Osawa, et al., Single-stranded DNA-packaged polyplex micelle as adeno-associated-virus-inspired compact vector to systemically target stroma-rich pancreatic cancer, ACS nano 13 (2019) 12732–12742.
- [53] D. Jiang, I. Rauda, S. Han, S. Chen, F. Zhou, Aggregation pathways of the amyloid  $\beta$ (1–42) peptide depend on its colloidal stability and ordered  $\beta$ -sheet stacking, Langmuir: ACS J. Surf. Colloids 28 (2012) 12711–12721.
- [54] A. Zabihollahpoor, M. Rahimnejad, G. Najafpour, A.A. Moghadamnia, Gold nanoparticle prepared by electrochemical deposition for electrochemical determination of gabapentin as an antiepileptic drug, J. Electroanal. Chem. 835 (2019) 281–286.
- [55] B.-A. Mei, O. Munteshari, J. Lau, B. Dunn, L. Pilon, Physical interpretations of Nyquist plots for EDLC electrodes and devices, J. Phys. Chem. C. 122 (2018) 194–206.
- [56] B. Tri Murti, Y.-J. Huang, A. Darumas Putri, C.-P. Lee, C.-M. Hsieh, S.-M. Wei, et al., Free-standing vertically aligned tin disulfide nanosheets for ultrasensitive aptasensor design toward Alzheimer's diagnosis applications, Chem. Eng. J. 452 (2023), 139394.
- [57] R. Fayazi, M. Habibi-Rezaei, M. Heiat, F. Javadi-Zarnaghi, R.A. Taheri, Glycated albumin precipitation using aptamer conjugated magnetic nanoparticles, Sci. Rep. 10 (2020) 10716.
- [58] K. Murakami, Y. Obata, A. Sekikawa, H. Ueda, N. Izuo, T. Awano, et al., An RNA aptamer with potent affinity for a toxic dimer of amyloid  $\beta$ 42 has potential utility for histochemical studies of Alzheimer's disease, J. Biol. Chem. 295 (2020) 4870–4880.
- [59] Y. Zheng, P. Wang, S. Li, X. Geng, L. Zou, M. Jin, et al., Development of DNA Aptamer as a  $\beta$ -Amyloid Aggregation Inhibitor, ACS Appl. Bio Mater. 3 (2020) 8611–8618.



**Masoud Negahdary** is a postdoctoral researcher at the Institute of Chemistry, University of São Paulo (USP), Brazil (2021-present). He received his Ph.D. (Clinical Biochemistry) from Yazd University of Medical Sciences, Iran (2018). His doctoral thesis and other main biosensing research were performed at the Nanomedicine and Nanobiology Research Center, Shiraz University of Medical Sciences, Iran (2015-2019).



**Thiago Regis Longo Cesar da Paixão** served as an Assistant Professor at the University Federal of ABC before joining the University of São Paulo in 2011 and was promoted to Associate Professor in 2016. 2018 the Brazilian Academy of Science recognized him as a promising young researcher. His research focuses on chemical sensors.



**William B. Veloso** graduated in Chemistry (2018) from the Federal University of Maranhão, received his M.Sc. (2021) from the same University and is currently a Ph.D. candidate in Chemistry at the University of São Paulo (Brazil). He has worked mainly on fabrication techniques for electrodes and analytical methods.



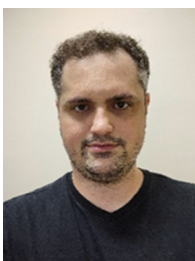
**Claudimir Lucio do Lago** is a full professor at the Institute of Chemistry, University of São Paulo (Brazil). His areas of interest include the development of instrumentation and analytical methods with an emphasis on capillary electrophoresis. He has published over 120 scientific articles, as well as chapters in books. He is a member of the editorial board of the *Hardware journal*.



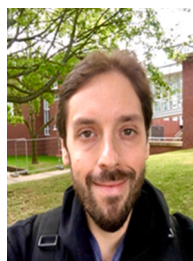
**Raphael P. Bacil** is currently a post-Doc Fellow within the institute of Chemistry of the University of São Paulo. His research interests include Molecular Electrochemistry, Electrocatalysis and Electroanalysis. He is also a member of the Brazilian Society of Electrochemistry (SBEE), and the International Society of Electrochemistry (ISE).



**Solange K. Sakata** is a Senior Research Investigator and the chair of the Graphene Nanocomposite Laboratory at the Radiations Technology Center, which is part of the Nuclear and Energy Research Center. She obtained her PhD in Chemistry from the University of São Paulo and completed her post-doctoral training in Biotechnology at the University of California, San Diego, USA. She was also a visiting researcher at the Fraunhofer Institute for Interfacial Engineering and Biotechnology in Germany.



**Rafael Martos Buoro** Obtained his Ph.D. in 2014 at the University of São Paulo under the supervision of Prof. Silvia Helena Pires Serrano with one year abroad period under the supervision of Prof. Ana Maria Oliveira Brett at FCTUC – Universidade de Coimbra in 2013. He is a Professor at the Departamento de Química e Física Molecular – IQSC – Universidade de São Paulo since 2016.



**Gabriel N. Meloni** has a B.Sc. (2012) and a Ph.D. (2017) in Chemistry from the University of São Paulo, USP (Brazil). He was a Marie Curie Research Fellow at the University of Warwick (UK, 2018-2020). He is currently a postdoctoral researcher at USP, working on the development of electrochemical devices.



**Ivano G. R. Gutz** received his Ph.D. in analytical chemistry in 1978 at the University of São Paulo, where he is full professor at the Institute of Chemistry since 1992. His research interests include electroanalytical chemistry, analytical instrumentation and automation.



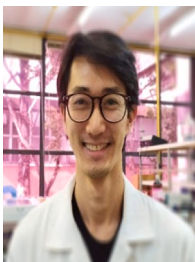
**Mesaque C. França** graduated in Chemistry from the Federal Institute of Maranhão (2016), received his M.Sc. from the Federal University of Maranhão (2021), and is currently a Ph.D. candidate in Chemistry at the Federal University of Ceará (Brazil). He worked mainly on the synthesis of materials for applications in electrochemical sensors. He is currently developing research at IQ-USP in electrocatalysis.



**Thawan Gomes de Oliveira** graduated in Bachelor of Chemistry from the University of São Paulo - IQUSP (2021), during this period, he developed activities as a student of scientific initiation (FAPESP) in the area of Physical Chemistry, with emphasis on Electrochemistry. He is currently a master's student at IQ-USP, working with flow injection analysis (FIA) for drug quantification.



**Michelangelo Durazzo** Is a researcher at IPEN in Materials Engineering with a focus on nuclear materials. Specialized in the physical characterization of materials, including scanning electron microscopy, optical microscopy, image analysis, X-ray diffraction, and thermal analysis; also a professor in the Nuclear Technology program at the University of São Paulo, USP/PEN.



**Wilson Akira Ameku** has Bachelor's and Ph.D. in chemistry from the University of São Paulo and a postdoctoral from the Oswaldo Cruz Foundation (FIOCRUZ). He worked on developing electrochemical biosensors and sensors for application in samples of forensic interest. He is currently a postdoctoral fellow at the University of São Paulo, working on developing low-cost, portable electrochemical biosensors.



**Lúcio Angnes** is a full professor at the Institute of Chemistry of the University of Sao Paulo. His research interests include the construction of electrodes with new and alternative materials, development of modified electrodes, arrays of microelectrodes, the design of different procedures of aptamer immobilization, and association of the created devices with bioanalysis systems. He is a member of the Sao Paulo State Academy of Science.